Electronic Supplementary Information

Inhomogenous doping induced nanocrystals imperfect self-assembled to synthesis of porous AgPb$_{10}$BiTe$_{12}$ nanosheets and their thermoelectric transport properties

Qun Wang,[*] Yuanyuan Fang, Hang Yin and Jianjun Li[*]

Department of Chemistry and National Key Laboratory of Science and Technology on Advanced

Composites in Special Environments, Harbin Institute of Technology, 92 West Dazhi Street, Harbin

150001, P. R. China

*To whom correspondence should be addressed. E-mail: wangqun5992@hit.edu.cn

Contents

1. Experimental Details

1.1 Materials and Preparation Procedures.

All chemicals are analytical grade and were directly used as received without further purification. In a typical procedure, 1.44 mmol of sodium tellurite (Na_2TeO_3), 1g KOH and 20 mL triethanolamine (TEA) were mixed to form a homogeneous solution under vigorous stirring in ambient. After stirring for 15 min, 0.12 mmol of $AgNO_3$, 1.20 mmol of $Pb(CH_3COO)_2 \cdot 3H_2O$, 0.12 mmol of $Bi(NO_3)_3 \cdot 5H_2O$ powders were added. And then, 5 mL of concentrated hydrazine hydrate $N_2H_4 \cdot H_2O$ (80%) solution were introduced into the above solution to form a clear solution. (Caution: hydrazine is highly toxic and should be handled with extreme care). With good mixing, the final solution was transferred into a Teflon-lined stainless-steel autoclave with a capacity of 50 mL, which was then filled with distilled water up to 70% of the total volume. Hydrothermal synthesis lasted for 18 h under the saturated water vapor pressure at 180 °C. Afterward, the autoclave was cooled down to room temperature. The black precipitates were filtered, cleaned with distilled water repeatedly, and eventually dried at 60 °C in a vacuum oven for 24 h. The specimens were then collected, in preparation for analysis and characterization.

1.2 Characterization.

The Powder X-ray diffraction (XRD) measurements were performed on a Rigaku Dmax 2000 X-ray diffractometer with Cu Kα radiation (λ= 0.154178 nm), in 2θ ranging from 10º to 80º. The microstructure and composition analyses were conducted on a field emission scanning electron microscope (FESEM, FEI QUANTA 200F) working at 30 kV. Transmission electron microscopic (TEM) images and high-resolution transmission electron microscopy (HRTEM) images were taken on a transmission electron microscope (TEM, FEI Tecnai G2) equipped with an energy-dispersive X-ray spectrometer (EDS) working at 300 kV. For typical SEM sampling, 1 mg product was added into 5 mL of absolute ethanol and then sonicated for 10 min to achieve a homogeneous suspension. The suspension can stay stable for several days without obvious settling at the bottom of the container. The suspension was then dropped onto a smooth silicon wafer substrate using a pipet for SEM measurement and onto carbon coated 200 mesh Cu grids for TEM, HRTEM and EDX characterization. Raman spectroscopy was recorded (Horiba Jobin Yvon CO. Ltd) using a 632.8 nm laser with an incident power of 5 mW. BET specific surface areas and pore volumes were calculated

from nitrogen adsorption-desorption isotherms determined at 77 K using an AUTOSORB-1-MP surface analyzer (the sample was outgassed under vacuum at 200 °C).

1.3 Thermoelectric transport properties

The black powder of $AgPb_{10}BiTe_{12}$ products treatment by N_2H_4 were pressed into compact bar-shaped samples ($10 \times 4.6 \times 1.0$ mm^3) by cold pressing under a high pressure of 20 MPa for electrical property measurements. Silver pastes were used as electrical contacts of the electrodes to the specimen. The electrical conductivities of the samples were measured by a DC four-probe technique using a 2400 sourcemeter (Keithley 2400, Keithley Instruments Inc., America) under an argon atmosphere from room temperature to 500 °C, in order to avoid possible oxidization at high temperature. To obtain the Seebeck coefficient, a microheater that created a temperature difference of about 3-15 K between the cool and hot ends of the specimen was applied. A temperature gradient was established in the samples when the electrical power was applied by a thermoelectric pile. The two thermocouples were contacted with the surface of the samples to detect the temperature drop (DT). The temperature and temperature differences (ΔT) were determined by calibrated nickel chromium-nickel silicon thermocouples, while the corresponding thermally induced voltage ΔV was recorded by the voltage probes. Then the Seebeck coefficient can be obtained by the formula, $S = -\Delta V/\Delta T$. The thermal conductivity was calculated from $\kappa = D \cdot C_p \cdot \rho$, where the thermal diffusivity coefficient D was measured using the laser flash diffusivity method on a Netzsch LFA457 (Netzsch, Selb, Germany) instrument. The temperature dependence of the heat capacity (C_p) was measured by a relaxation method using a Quantum Design physical properties measurement system (PPMS). The density (ρ) is 6.62 g/cm^3.
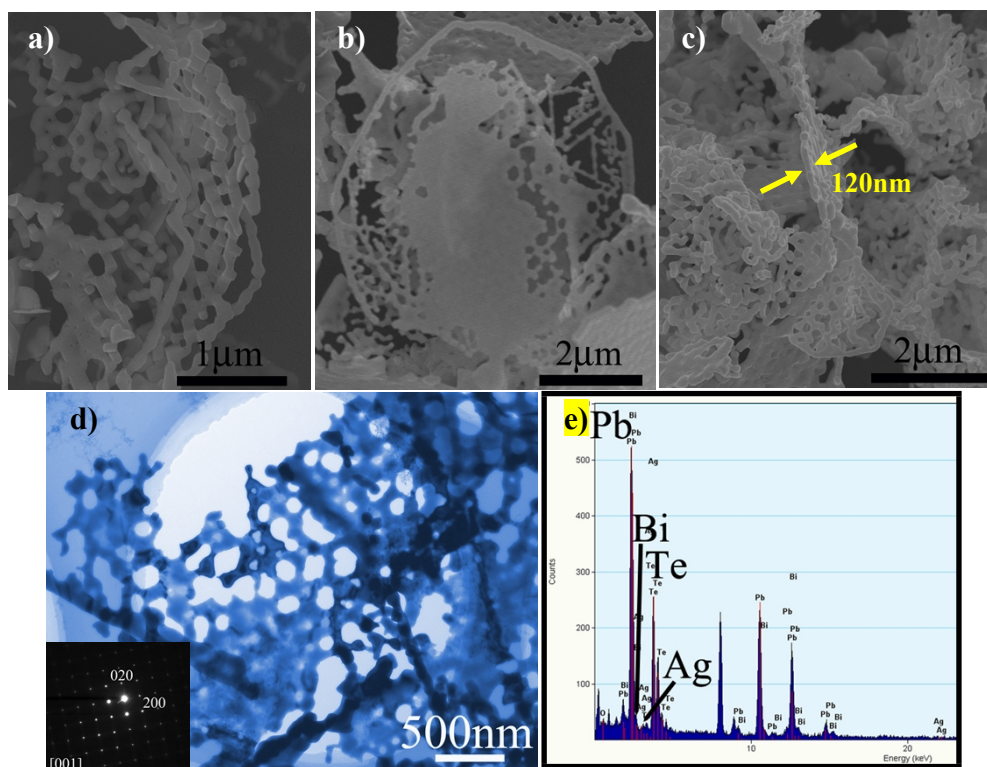
Fig. S1 (a-c) SEM images, (d) TEM image and the inset SAED pattern, displaying only one set of reciprocal spots and (e) EDX spectrum of the AgPb$_{10}$BiTe$_{12}$ product. It was found that the obtained products possess a 2D meso/macroporous sheet-like morphology.
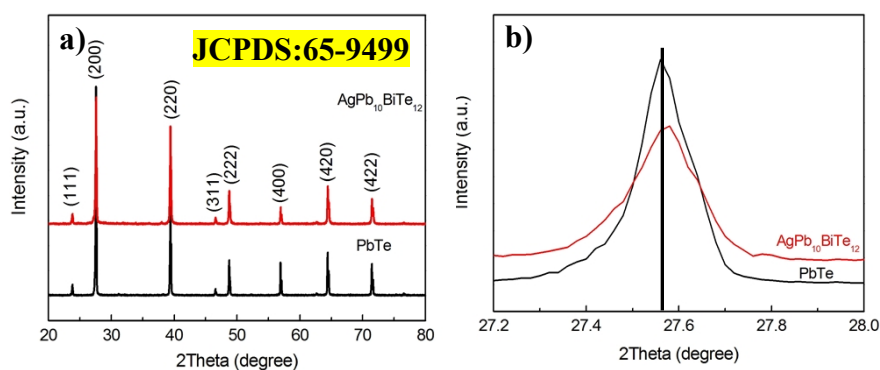
Fig. S2 (a) Powder X-ray diffraction patterns of the AgPb$_{10}$BiTe$_{12}$ nanosheets and PbTe product fabricated by using the same method. No extra lines corresponding to Bi, Ag, Pb, corresponding oxides, or binary tellurids phases, suggesting that there is no phase separation in the nanoparticles. (b) XRD patterns for the two samples where 2θ ranges from 27° to 28°. The smaller Ag and Bi cations are introduced in the host PbTe lattice, leading to the shift of the peaks of the pattern to higher 2θ values.

As shown in Fig. S3a, it is well known that NaCl-type crystal structure of PbTe, where all the atoms at the center of the symmetry ($O_h{}^5$), all q≈0 vibrational modes are Raman inactive. In spite of this restriction, it may be possible to observe Raman scattering since actual synthesized materials are often not of perfect crystalline structure, especially for extrinsic doping. Any deviation from a perfect crystal, such as nonstoichiometry, deformation, dislocations, or extrinsic doping, could cause vibrational modes to be Raman active.[1, 2] We performed Raman spectroscopy measurements here to investigate how the compositional variations due to doping affect the lattice vibrations and the electron phonon interactions in porous nanosheets. The vibrational mode at 122 cm^{-1} is assigned to the LO phonon of the PbTe due to uncompensated Te atoms in the *fcc* NaCl-type lattice of PbTe, which is bigger than the value for unstrained PbTe bulk crystals (119 cm^{-1}) by surface electric-field-induced Raman scattering. The residual strain in the porous nanosheets is responsible for the observation of the PbTe LO phonon. In addition, two clearly resolved peaks at ~135 cm^{-1} and ~171 cm^{-1} are seen in the spectrum, suggesting these peaks are actually oxide-related. The former is typically assigned to the Pb-O-Pb symmetrical stretch.[3]

A significant amount of oxygen is usually observed at the surface of PbTe NPs when exposed to air even during very short periods of time.[4,5] In our case, large surface-to-volume ratio of nanosheet shows high reaction reactivity with O_2, because the more dangling bonds of bare and uncoordinated metal sites (Pb, Bi) may exist due to extrinsic doping. Recently, Garcia-Gutierrez et al. showed that the synthesized nanoparticles always display a higher concentration of Pb compared to that of the chalcogen, which is related to the excess of Pb observed on the surface of the nanoparticles.[6] Therefore, the surface of product is covered by the amorphous thin oxide layer.

In Fig. S3b, the textural characteristic of as-prepared products is investigated by the gas sorption measurement at 77 K. The nitrogen adsorption−desorption isotherm of the sample is shown in Fig. S3b, and the inset shows the Barrett−Joyner−Halenda (BJH) pore size distributions obtained from the absorption branch. This isotherm profile can be categorized as type IV with a small hysteresis loop observed at a relative pressure of 0.5−1.0, indicating the presence of a wide distribution of meso/macroporous structure in the sample. It can be seen from the pore size distribution that the porous nanosheets have a wide pore-size distribution ranging from 5 to 100 nm. As expected, the sample has a high specific surface area of 122 m^2 g^{-1}. The high BET surface area

and large total pore volume strongly support the fact that the prepared products have a porous structure. This result is in agreement with the SEM and TEM observations.
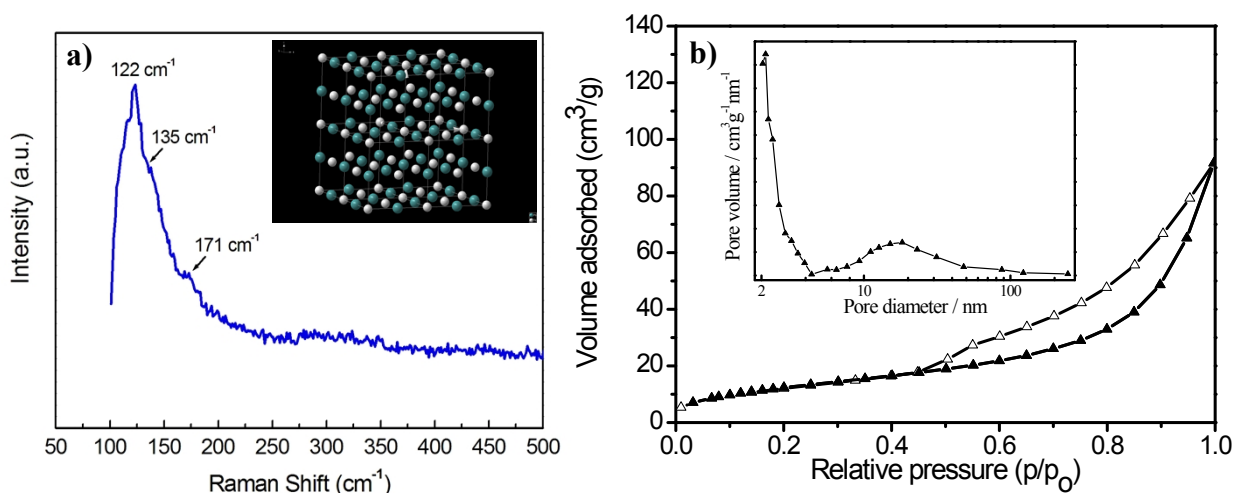

Fig. S3 (a) Raman spectrum and (b) N_2 adsorption-desorption isotherms and the corresponding Barrett-Joyner-Halenda (BJH) pore-size distribution plots of porous nanosheets. It was found that the pores distributed in the porous sheet-like products possess a wide pore size distribution rang from 5 to100 nm.

Ag: Pb: Bi: Te = 0.33: 8.91: 2.00: 11.15

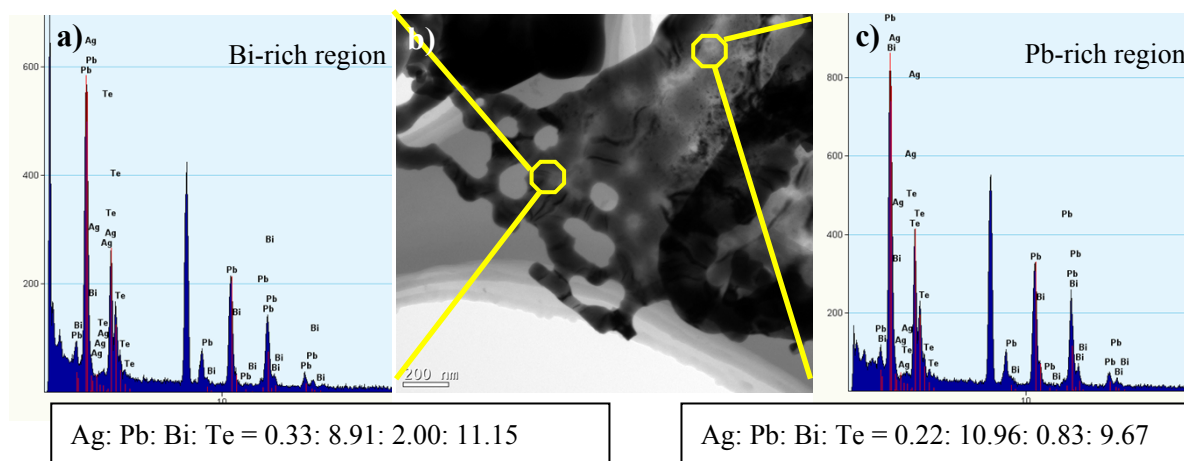Ag: Pb: Bi: Te = 0.22: 10.96: 0.83: 9.67

Fig. S4 EDX spectra of the porous nanosheet collected at different positions. These results suggest that the Ag component is low and Bi-rich region around the edge of the pore appeared.
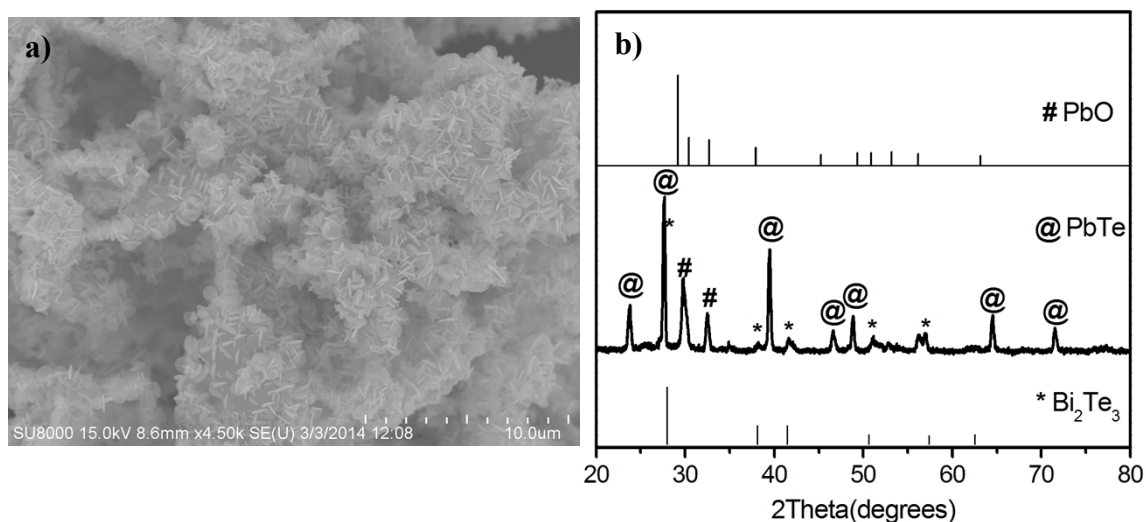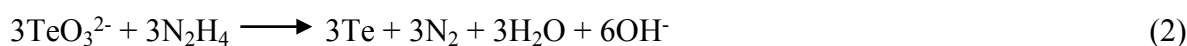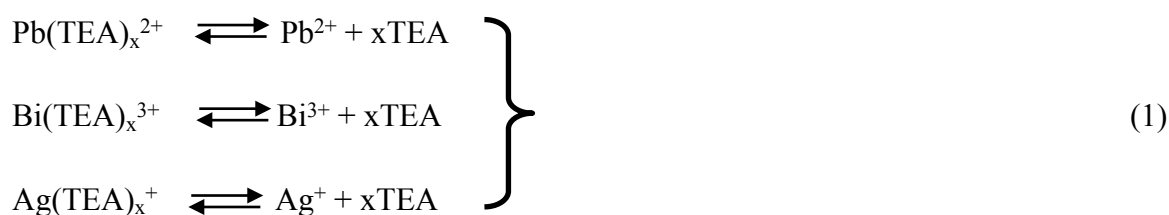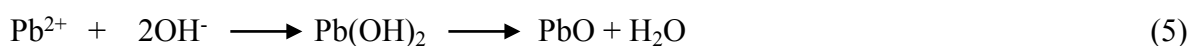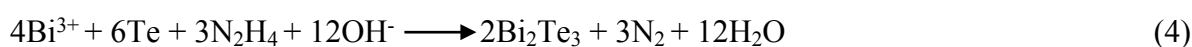
Fig. S5 (a) SEM image of product obtained at high Bi content (0.24 mmol) and (b) XRD patterns. From this figure, we interpret the results as follows: in thermodynamic terms, the solubility product (Ksp) of an ionic solid is referred to as an equilibrium constant between an ionic solid and its dissolved state. Ions in a solid with a relatively lower solubility are favorable to form. The relative order in the solubility products of $Ksp(Bi_2Te_3)<Ksp(PbTe)$. The most reactive (Bi) precursor quickly reacts (with Te) to homogeneously Bi_2Te_3 nuclei; the less reactive Pb precursors subsequently react to PbTe. At last, the remained Pb reacts with OH to produce oxides.

Since triethenthmine (TEA) is a strong ligand with three -OH groups and one amine group and has high nucleophilic nature, Pb^{2+} Bi^{2+}, Ag^{2+} or corresponding oxides could interact with TEA molecules to form a $Pb(TEA)_2^{2+}$, $Bi(TEA)_3^{3+}$, $Ag(TEA)^+$ organometallic complex.[7, 8] Thus, the overall chemical reaction involved in the hydrothermal synthesis can be described by the following eqs 1-5:

$$Pb(TEA)_x^{2+} \rightleftharpoons Pb^{2+} + xTEA$$

$$Bi(TEA)_x^{3+} \rightleftharpoons Bi^{3+} + xTEA \qquad (1)$$

$$Ag(TEA)_x^+ \rightleftharpoons Ag^+ + xTEA$$

$$3TeO_3^{2-} + 3N_2H_4 \longrightarrow 3Te + 3N_2 + 3H_2O + 6OH^- \qquad (2)$$

$$2Pb^{2+} + 2Te + N_2H_4 + 4OH^- \longrightarrow 2PbTe(Bi,Ag) + N_2 + 4H_2O \qquad (3)$$

High Bi concentration:

$$4Bi^{3+} + 6Te + 3N_2H_4 + 12OH^- \longrightarrow 2Bi_2Te_3 + 3N_2 + 12H_2O \qquad (4)$$

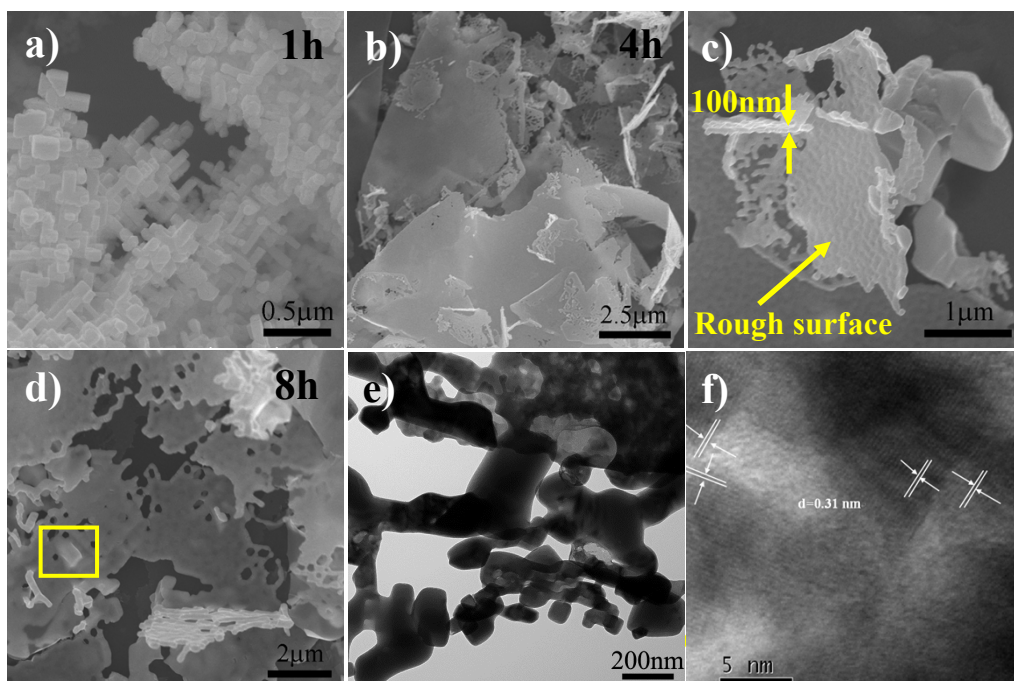$$Pb^{2+} + 2OH^- \longrightarrow Pb(OH)_2 \longrightarrow PbO + H_2O \qquad (5)$$

Fig. S6 The morphological evolution of the samples prepared at 180 ° C for different reaction times: a) 1 h; b-c) 4 h; d-f) 8 h.
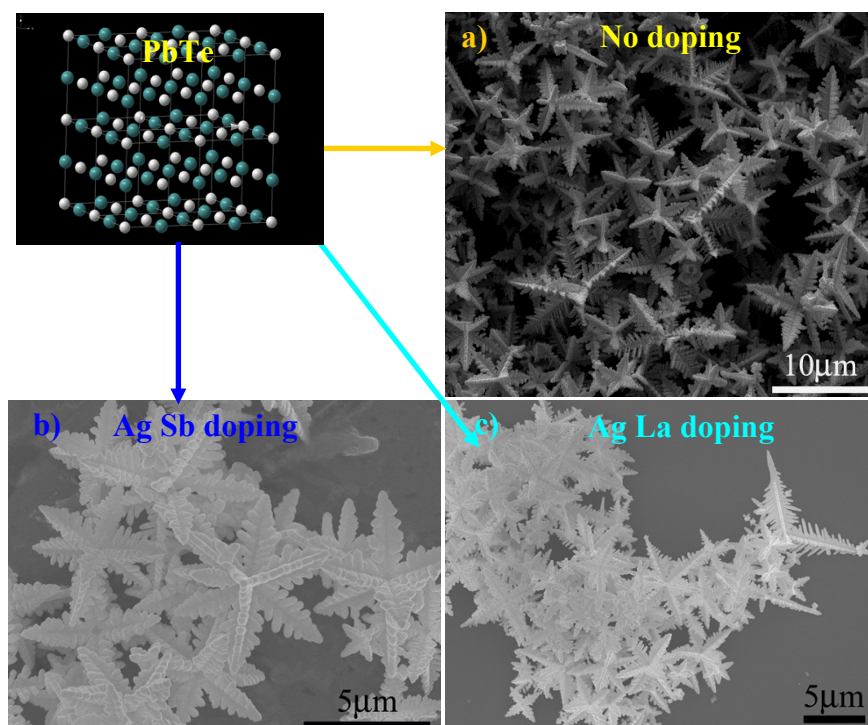
Fig. S7 (a) SEM images of the products obtained in the absence of Ag, Bi dopants and (b, c) Ag, Bi was substituted by Ag, M = Sb, La under identical experimental condition, respectively.

Fig. S8 (a-c) SEM images of the products fabricated at different reaction temperature. It can be seen that the high temperature is favorable to the appearance of pores throughout the nanosheets. Similar phenomenon was reported in Sb_2Te_3 nanorings, which were achieved by dissolution of the inner part with a higher density of defects of the hexagonal nanoplates.[9]

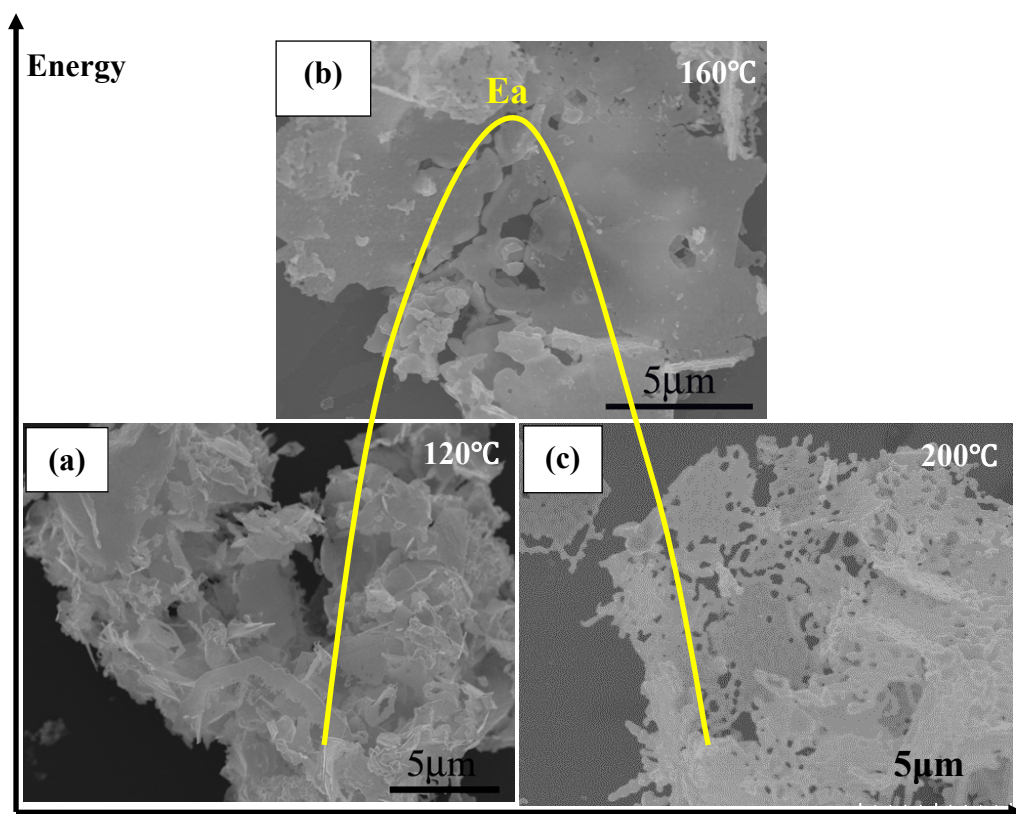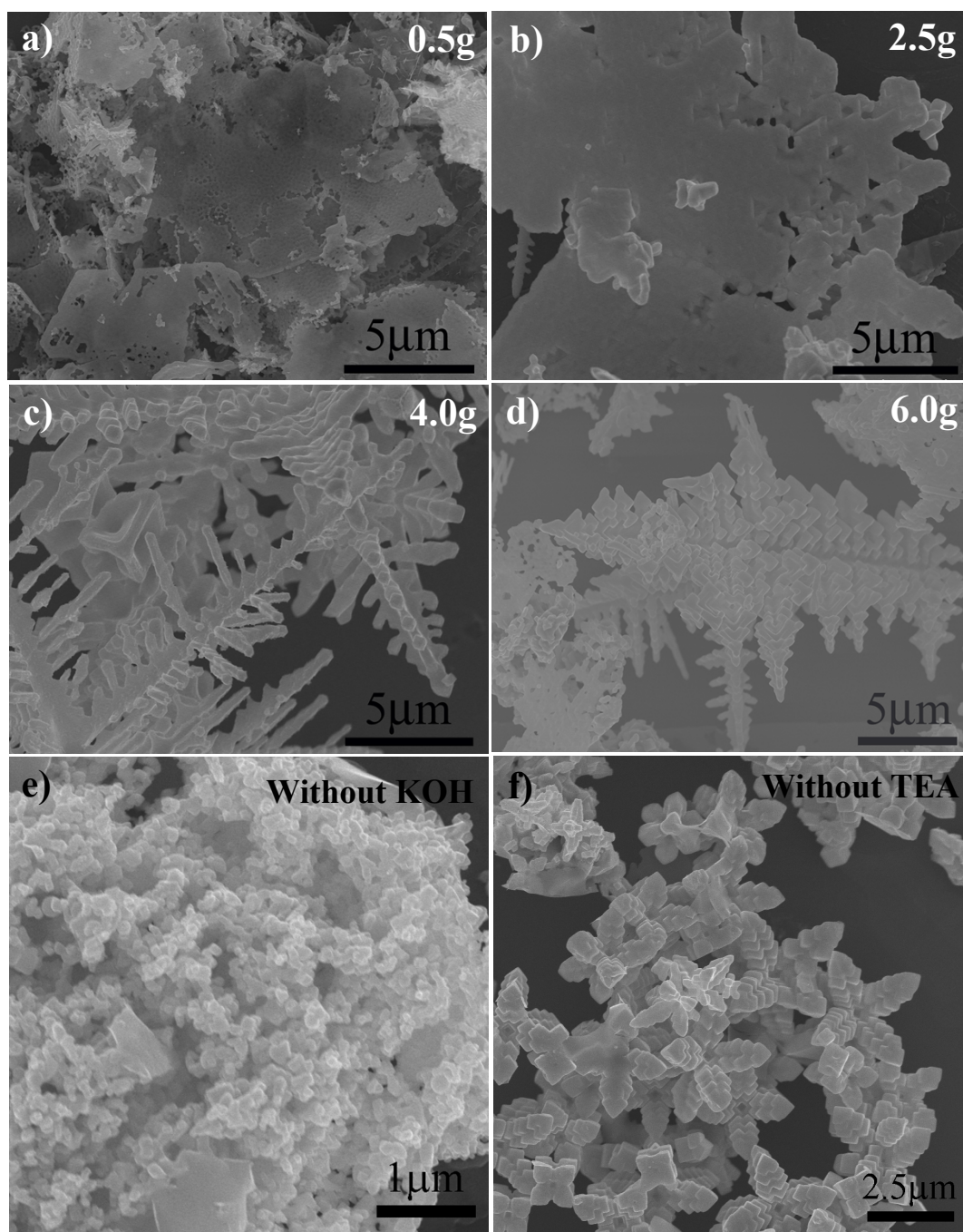**Fig. S9** (a-e) SEM images of the products collected at different KOH amount and (f) in the absence of TEA. The observed broken plates may arise from KOH etching at defect sites, i.e., in the center of the plate. When the KOH concentration is low (<2.5g), the reaction rate of synthesized product is very slow, which is favorable to formation of sheet-like structures. On the other hand, it is well-known that alkaline solution was used for producing dislocation etch pits on PbTe crystal in the previous literature and thus the freshly prepared PbTe nanocrystals can be soluble in hot alkaline solution.[10] Therefore, when the KOH concentration is too high (>4g), the freshly formed PbTe seeds can be dissolved quickly and undergo a different chemical reaction route to form dendrite crystals.
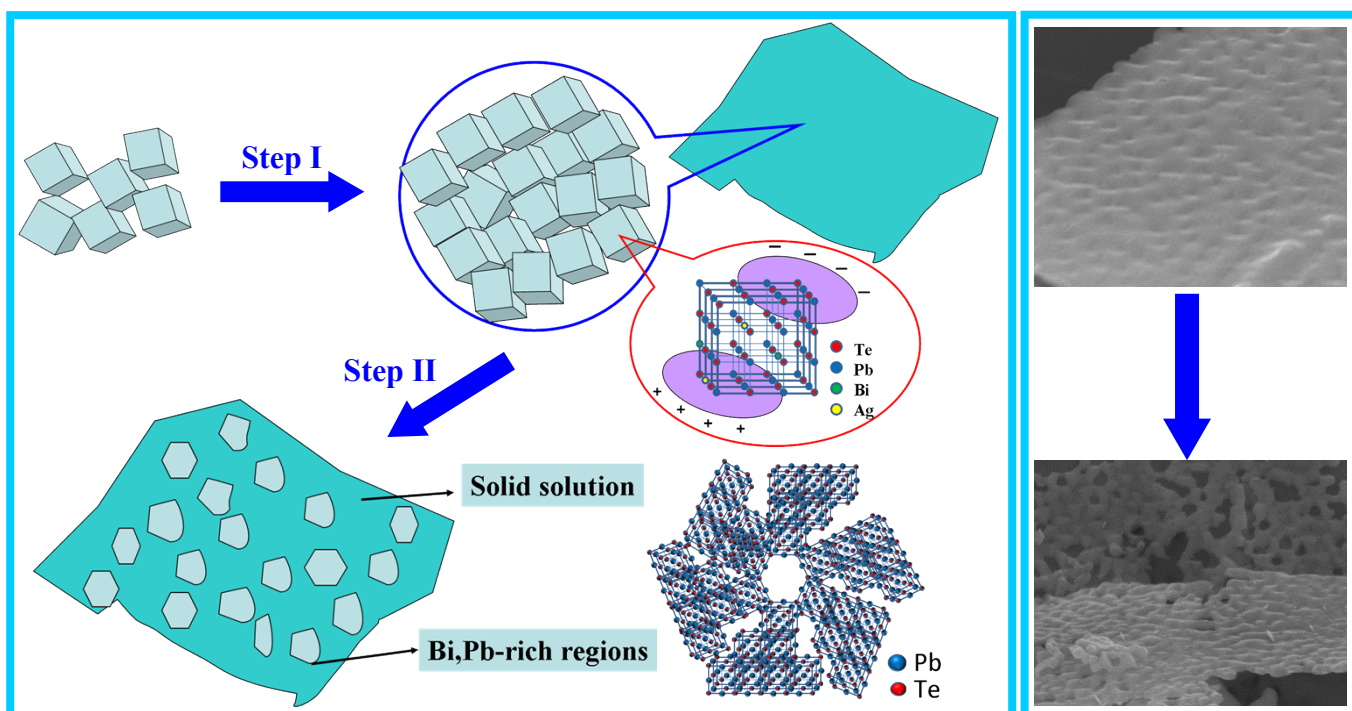
Scheme 1. Schematic illustration for the formation process of porous nanosheets. At step I, spatial redistribution of Ag, Bi atoms in the PbTe crystal lattice caused the electron charge density of the cubic crystal surface variation. Therefore, some nanocubes rotate and have disordered assemblies due to anisotropic dipolar NP-NP interactions, which provide a reasonable explanation for the observed rough surface with some pits of the nanosheet prepared for 4h. This may explain the HRTEM result in Fig. 3c which displays the two series of lattice fringes appeared in the selected area. Then each crystal particle incompletely coalesces together and leaves the vacant porous sites between interconnected NPs [11] to form nanosheets with different shaped nanopores (including hexagonal or pseudo hexagonal pores) observed in this study. The inset illustrated that hexagonal pore was constructed by disorder attachment of several nanocubes.
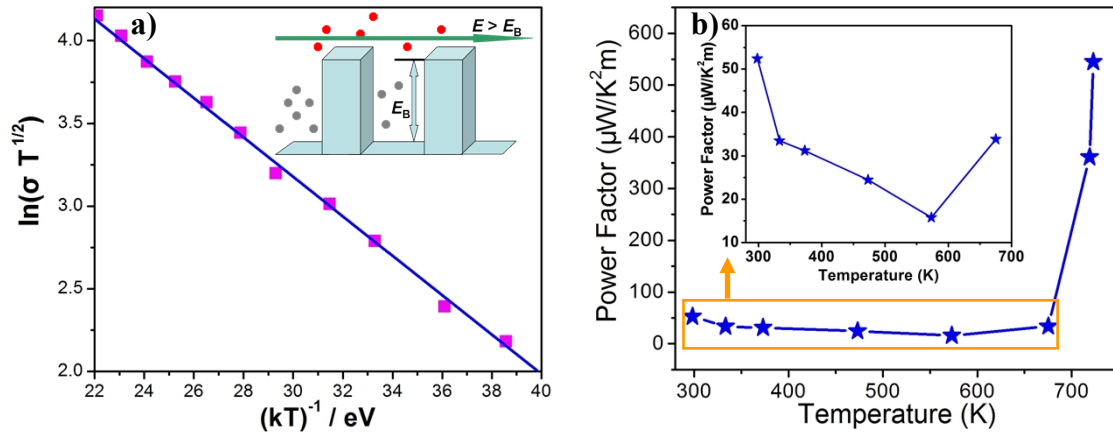
Fig. S10 Thermoelectric properties as a function of temperature for samples. (a) Plot of $\ln(\sigma T^{1/2})$ vs $1/(kT)$ for samples, along with a fit to Equation $\sigma(T) \sim (1/(T)^{1/2}) \exp(-E_B/k_B T)$ to derive the energy barrier associated with grain boundary potential barrier scattering. Activation energy of about 118 meV was obtained from the linear fitting and (b) Power factor. The inset in (a) representation of the trapping of low energy charge carriers (green solid circle) at the grain boundaries, red solid circle represents higher energy charge carriers capable of overcome the grain boundary potential barrier,
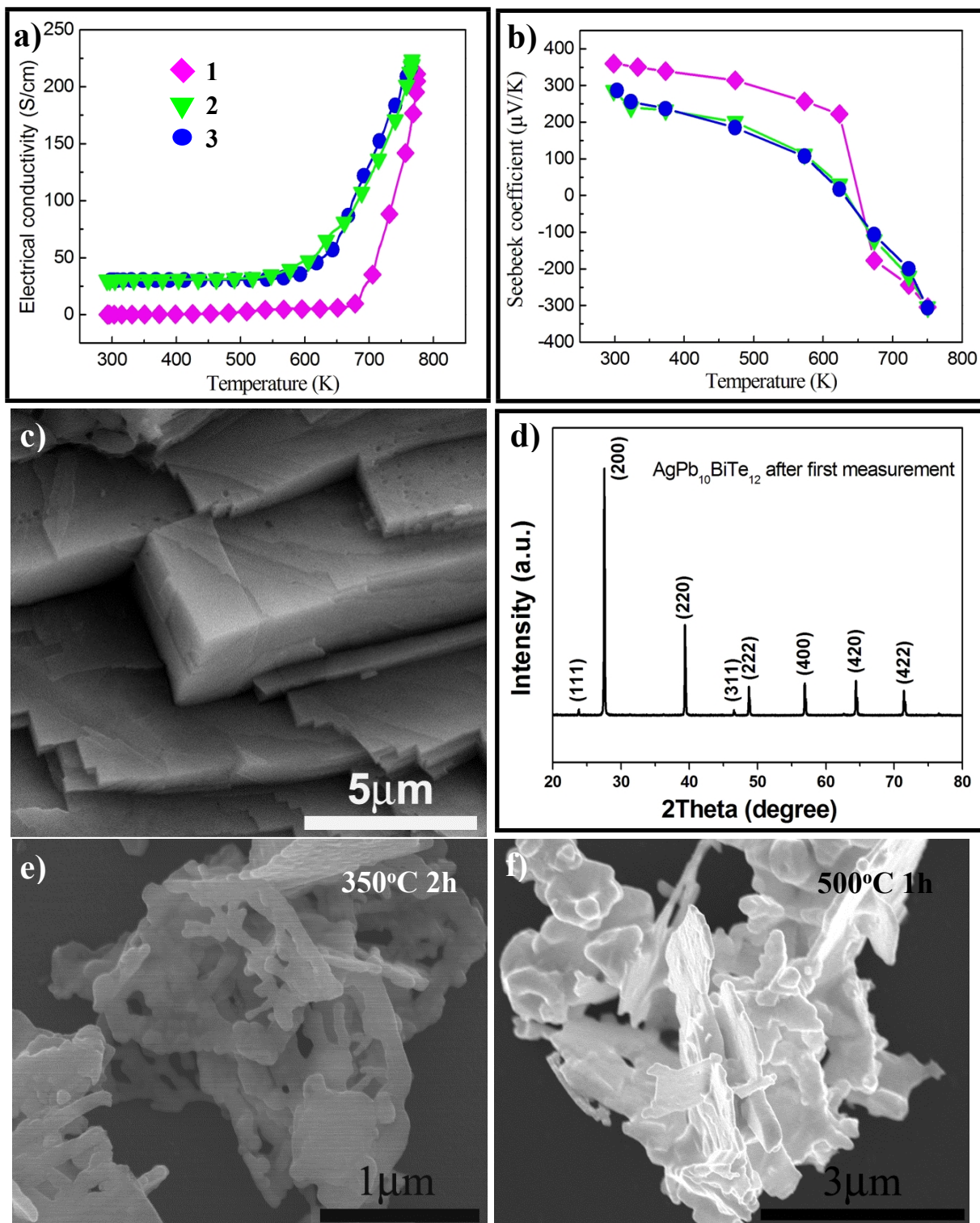
Fig. S11 Multiple measurements of the electrical conductivity (a) and Seebeck coefficient (b), SEM image shows intergranular fracture image of the $AgPb_{10}BiTe_{12}$ bulk obtained after first measurement (c), demonstrating that it is very dense and the morphology is very different from the starting porous nanosheets. Powder X-ray diffraction patterns of $AgPb_{10}SbTe_{12}$ collected after the measurement of electrical conductivity (d), SEM image of $AgPb_{10}BiTe_{12}$ porous nanosheets at different sintering temperature under N_2 atmosphere: 350 °C for 2h (e) and 500 °C for 1h (f).

Recently, Nolas et al. observed transport properties of PbTe nanocomposites prepared from solution-phase synthesized PbTe nanocrystals have a strong sensitivity to stoichiometry, surface oxygen adsorption, and porosity (density).[12] It is well known that nanomaterials' stability and measurement reproducibility are major concerns, particularly in bottom-up-assembled nanocomposites. The thermoelectric performance stability of the nanocomposites by measuring the materials' thermoelectric properties multiple times was tested. An enhanced electrical conductivity at low temperature was seen after the first measurement (see Fig. S11 a, b), and then thermoelectric properties remained unchanged. The changes between the first and next cycles may origin from a slight loss of tellurium, which can be explained by the phase diagram of the Pb−Te system as well as the temperature dependence of the vapor pressure of Te. Similar changes of electrical conductivity were also observed in $(PbTe)_{0.28}(PbS)_{0.72}$ nanocomposites by Cabot's research group (ref.13 in the main text). However, the actual effect of annealing on electrical conductivity is unknown since it must be pointed out that such potential tellurium loss was not detected by ICP or EDX. Of course, it is not exclude that grain growth will occur when the small size (several nm) grains are subjected to high temperatures. However, larger size (tens of nm or larger) domains in $AgPb_{10}BiTe_{12}$ should have enough resistance against the thermal ripening at high temperatures, especially for short heat treatment time. Therefore, not all nanomaterials are thermodynamically unstable (ref.14 in the main text). It is meaningful to investigate the possible effect of several post-treating strategies, including annealing, pressing, and sintering, for fabricating nanostructured bulk materials from the compaction of nanoparticles on the thermoelectric properties [13]. We have detected the XRD of sample collected after the first measurement of electrical conductivities. As seen in Fig. S11 d, there are no apparent changes of crystal structure and purity of the samples were detected after first measurement, which represents the samples all possess typical cubic phases as the specimen before measurement. However, SEM image of the cross-section of bulk bar after first measurement clearly showed that the porous structure disappeared and the bar was very dense (Fig. S11 c). In addition, SEM images of $AgPb_{10}BiTe_{12}$ porous nanosheets at different sintering temperature (350 $^{\circ}$C for 2h and 500 $^{\circ}$C for 1h) under N_2 atmosphere were investigated (Fig. S11 e, f), showing an influence of sintering temperature on the morphology of porous nanosheets. We believe that the enhanced ZT value in our sample could be possible if one can make high density bulk samples through some special techniques, such as sparking plasma sintering (SPS) process, making it possible to prevent unwanted grain

growth arising from a long sintering process at high temperatures.[13] Future work will aim to investigate the influence of the consolidation conditions including pressure, temperature and time on the properties of nanocomposites.

Supplementary References:

[1] M. Baleva and M. Momtchilova, *Phys. Rev. B* 1994, **50**, 15056

[2] H. Wu, C. Cao, J. Si, T. Xu, H. Zhang, H. Wu, J. Chen, W. Shen and N. Dai, *J. Appl. Phys.* 2007, **101**, 103505.

[3] J. L. Blackburn, H. Chappell, J. M. Luther, A. J. Nozik and J. C. Johnson, *J. Phys. Chem. Lett.* 2011, **2**, 599.

[4] M. Scheele, N. Oeschler, I. Veremchuk, S. O. Peters, A. Littig, A. Kornowski, C. Klinke and H. Weller, *ACS Nano* 2011, **5**, 8541.

[5] Y. Zhao and C. Burda, *ACS Appl. Mater. Interfaces* 2009, **1**, 1259.

[6] D. I. Garcia-Gutierrez, D. F. Garcia-Gutierrez, L. M. De Leon-Covian, M. T. Treviño-Gonzalez, M. A. Garza-Navarro, I. E. Moreno-Cortez and R. F. Cienfuegos-Pelaes, *J. Phys. Chem. C* 2014, **118**, 22291.

[7] W. T. Miller, *J. Am. Chem. Soc.* 1940, **62**, 2707.

[8] L. H. Lin, C. C. Wu and T. C. Lee, *Cryst. Growth Des.* 2007, **7**, 2725.

[9] W. Wang, D. Long, Y. Liang, G. Zhang, B. Zeng and Q. He, *Langmuir* 2011, **27**, 815.

[10] B. B. Houston and M. K. Norr, *J. Appl. Phys.* 1960, **31**, 615.

[11] Z. W. Wang, C. Schliehe, T. Wang, Y. Nagaoka, Y. C. Cao, W. A. Bassett, H. Wu, H. Fan and H. Weller, *J. Am. Chem. Soc.* 2011, **133**, 14484.

[12] J. Martin, L. Wang, L. Chen and G. S. Nolas, *Phys. Rev. B* 2009, **79**, 115311.

[13] H. Y. Fang and Y. Wu, *J. Mater. Chem. A*, 2014, **2**, 6004